Incomplete Initial Nutation Diffusion Imaging: An Ultrafast, Single-Scan Approach for Diffusion Mapping

Andrada Ianuş[1,2] and Noam Shemesh 🟢[1]*

Purpose: Diffusion MRI is confounded by the need to acquire at least two images separated by a repetition time, thereby thwarting the detection of rapid dynamic microstructural changes. The issue is exacerbated when diffusivity variations are accompanied by rapid changes in T_2. The purpose of the present study is to accelerate diffusion MRI acquisitions such that both reference and diffusion-weighted images necessary for quantitative diffusivity mapping are acquired in a single-shot experiment.
Methods: A general methodology termed incomplete initial nutation diffusion imaging (INDI), capturing two diffusion contrasts in a single shot, is presented. This methodology creates a longitudinal magnetization reservoir that facilitates the successive acquisition of two images separated by only a few milliseconds. The theory behind INDI is presented, followed by proof-of-concept studies in water phantom, ex vivo, and in vivo experiments at 16.4 and 9.4 T.
Results: Mean diffusivities extracted from INDI were comparable with diffusion tensor imaging and the two-shot isotropic diffusion encoding in the water phantom. In ex vivo mouse brain tissues, as well as in the in vivo mouse brain, mean diffusivities extracted from conventional isotropic diffusion encoding and INDI were in excellent agreement. Simulations for signal-to-noise considerations identified the regimes in which INDI is most beneficial.
Conclusions: The INDI method accelerates diffusion MRI acquisition to single-shot mode, which can be of great importance for mapping dynamic microstructural properties in vivo without T_2 bias. **Magn Reson Med 79:2198–2204, 2018.** © 2017 The Authors Magnetic Resonance in Medicine published by Wiley Periodicals, Inc. on behalf of International Society for Magnetic Resonance in Medicine. This is an open access article under the terms of the Creative Commons Attribution License, which permits use, distribution and reproduction in any medium, provided the original work is properly cited.

Key words: diffusion; magnetic resonance imaging; isotropic encoding; ultrafast MRI; mean diffusivity

INTRODUCTION

Methods enabling rapid acquisition of dynamic MRI data have greatly affected contemporary MRI. Functional MRI (1–5), hyperpolarized imaging (6), MR fingerprinting (7), and multidimensional NMR (8) are based on, and continuously benefit from, ultrafast acquisition schemes. In contrast, diffusion MRI (dMRI) methods (9), typically relying on single-diffusion-encoded schemes (10), are not usually acquired dynamically, but their ability to probe microarchitectural features such as anisotropy (11), complex fiber configurations (12,13), microscopic anisotropy (14–17), and cellular-scale dimensions (18–20) have made them widely applicable (21). A few examples include early stroke detection (22–24), white matter orientation mapping (25), studies of neuroplasticity (26), or detection of microstructural aberrations upon disease (27,28).

Rapid and dynamic determination of diffusion-derived metrics, however, is particularly important for diffusion functional MRI (dfMRI) [29, 30], a method aiming to detect neural activity through non-blood-oxygenation-level-dependent (BOLD) mechanisms. Diffusion functional MRI evidenced faster activation dynamics and more localized activation foci compared with BOLD, suggesting it may be more closely correlated with underlying neural activity (29–31). However, dfMRI's temporal resolution can be limited by the necessity to acquire at least two signals (one baseline image and one diffusion-weighted image) for quantifying the apparent diffusion coefficient. To avoid excessive T_1 weighting and severe degradation in image quality, dfMRI measurements are typically separated by at least repetition times (TRs) greater than 2 to 3 T_1, imposing a practical limit on temporal resolution. Additionally, T_2 variations can occur on the timescale of a typical TR, potentially biasing the measurement and complicating the interpretation of dfMRI (32,33).

Isotropic diffusion encoding (IDE) based dMRI has recently re-emerged as a valuable tool for speeding up the acquisition of a valuable rotationally invariant parameter of the full diffusion tensor: its mean diffusivity (MD). Isotropic-encoding schemes have been proposed, for example, by Mori and van Zijl, who suggested the application of consecutive gradients along the laboratory x-, y-, and z- gradients (34). Topgaard used a similar diffusion encoding in a triple stimulated echo sequence (35). De Graaf et al extended this idea to MR spectroscopy (36), and gradient

INDI methodology

FIG. 1. General INDI methodology. In this implementation, the sequence is furnished with isotropic diffusion-encoding gradients. The sequence begins with an incomplete initial nutation (in our case, $\alpha_x = \frac{\pi}{4}$). A spin echo then proceeds, with the first acquisition providing the $b = 0$ s/mm^2 image (in our implementation, an EPI acquisition, S_1). Bipolar spoiler gradients (shown here in black) are then applied to remove residual magnetization, while refocusing the residual phase to remove possible nuisance artifacts, in a similar manner to phase rewinding in typical ultrafast imaging. Here, T_{spoil} was on the order of approximately 1–10 ms. The second nutation pulse (here, $\beta_{-x} = \frac{\pi}{2}$) rotates the remaining fresh longitudinal magnetization for the next spin echo, which is acquired with exactly the same timing and parameters as the first echo, only the diffusion gradients are now applied (S_2). Here, we focus on obtaining the MD by applying IDE gradient waveforms. The resulting UF-IDE pulse sequence thus provides both baseline and diffusion-weighted images within $2TE + T_{EPI} + T_{spoil}$.

waveforms were optimized to improve IDE's efficiency (37). Other methods imparting different b-values within a single scan (which, however, requires averaging for phase cycling) by making different coherence pathways sensitive to different b-values have also been presented (38). More recently, Eriksson et al presented magic angle spinning of the q-vector, an elegant IDE framework harnessing harmonically modulated gradient waveforms (39) or numerically optimized waveforms (40).

Here, we present a method called incomplete initial nutation diffusion imaging (INDI), which is designed to obtain both a baseline and a diffusion-weighted image in a single shot without loss of signal-to-noise ratio (SNR) or temporal resolution. Nutation angles are tailored to keep a "fresh" longitudinal magnetization reservoir, such that it can be used for consecutive measurements separated by only a few milliseconds, mitigating potential biases in MD quantification as a result of time-varying T_2. The accuracy of INDI is validated in phantoms and in vivo on a preclinical system. Simulations analyzing INDI SNR considerations and future applications, especially via dfMRI, are discussed.

METHODS

The INDI method is presented in Figure 1, and its theory is presented in the Supporting Information. The INDI mode of operation is rather simple: A fraction of the magnetization is rotated from the equilibrium position using a nutation angle α, leaving (ideally) an equal magnetization pool unperturbed; a non-diffusion-weighted image is then

acquired. Immediately after this first acquisition, residual transverse magnetization is crushed, and all of the unperturbed magnetization in the "reservoir" is converted to transverse magnetization using a pulse angle β. An otherwise identical image to the previous excitation is acquired, but now the diffusion-weighting gradients are also applied (Fig. 1). Thus, the two images required for quantifying diffusion coefficients are acquired with a separation of only a few milliseconds dictated by the TE, the EPI acquisition time, and the spoiler duration (see Fig. 1).

All experiments involving animals were pre-approved by the institutional ethics committee. The phantom and ex vivo experiments were performed on a Bruker Aeon Ascend 16.4T scanner (Bruker, Karlsruhe, Germany) interfaced with an Avance IIIHD console and equipped with gradients capable of producing up to 3000 mT/m in all directions. In vivo experiments were performed on a Bruker BioSpec 9.4T scanner equipped with gradients capable of delivering up to 660 mT/m in all directions.

Specimen Preparation

Doped water phantoms were prepared by gradually adding copper sulfate to a 30/70% (volumetric) D$_2$O/water, until a longitudinal relaxation time of approximately 200 ms was obtained. The solution was placed in a 5-mm NMR tube, which was sealed and placed in a 10-mm NMR tube filled with Fluorinert (Sigma Aldrich, Lisbon, Portugal). Brain samples (n = 3) were extracted from healthy male C57bl mice weighing approximately 25 g by standard intracardial paraformaldehyde perfusion, followed by 12 h in a 4%

paraformaldehyde solution at $4\,^\circ$C, and placement in phosphate-buffered saline at $4\,^\circ$C. The brains were then soaked in a solution of phosphate-buffered saline and 0.5M gadoterate meglumine (Dotarem, Guerbet, Lisbon, Portugal) at a dilution of 1:200 (2.5 mM) for 12 h (41), washed with phosphate-buffered saline, and placed in a 10-mm NMR tube filled with Fluorinert. All samples were allowed to equilibrate with the surrounding constant temperature of $37\,^\circ$C.

Scout INDI Images

An INDI "scout" sequence was acquired once per specimen with all identical diffusion gradients turned off. These scouts were used to correct INDI-derived maps.

Water Phantom Experiments

Following the acquisition of routine localization images and shimming, the water phantom was subject to three types of experiments: a "ground-truth" DTI, a conventional IDE MRI experiment, and the ultrafast IDE (UF-IDE) sequence. All experiments shared the following acquisition parameters: single-shot echo-planar imaging (EPI), bandwidth $= 652173$ Hz, field of view $= 10 \times 10\,\text{mm}^2$, matrix size 80×80 (partial Fourier encoding of 1.33, double sampled), leading to an in-plane resolution of $125 \times 125\,\mu\text{m}^2$, with a slice thickness of $900\,\mu\text{m}$. The TR/echo time (TE) was 1800/20 ms. The UF-IDE and IDE diffusion gradient waveforms were generated according to (42) for isotropic encoding. Diffusion gradients (40) placed before the INDI's second refocusing pulse (Fig. 1) were nulled to minimize TE, which can be done since the waveforms are independent and self-refocusing the diffusion waveform following INDI's second refocusing pulse and had a duration of 7.5 ms and a b-value of 400 s/mm^2. The DTI experiments were performed using a pulsed-gradient spin-echo sequence with $\Delta/\delta = 4/2$ ms, and six diffusion-weighted images (b $= 400$ s/mm^2, gradients applied in non-collinear directions) and six additional baseline images (b $= 0$ s/mm^2) were acquired.

Ex Vivo Brain Experiments

In the brain samples, IDE and UF-IDE experiments were performed with identical acquisition parameters as described previously for the water phantom, but with the following modifications: slice thickness $= 650\,\mu\text{m}$ (six slices), b $= 1000$ s/mm^2, and TR $= 2500$ ms; no double-sampling was used.

In Vivo Experiment

A male C57bl mouse weighing approximately 25 g was anesthetized with isoflurane (4% induction, 1–2% maintenance in 95% O_2) and placed in the scanner. A closed-loop circulating water system was used for temperature regulation, and respiration and rectal temperature were monitored continuously. Transmission was achieved through an 86-mm quadrature resonator, and the signal was detected by a four-element array receive-only cryo-cooled coil (Bruker, Fallanden, Switzerland). The UF-IDE and IDE experiments were performed using the following common parameters: fat-suppressed single-shot EPI, bandwidth $= 326087$ Hz, field of view $= 16 \times 12\,\text{mm}^2$, matrix size 106×80 (partial Fourier encoding of 1.25), leading to an in-plane resolution of $150 \times 150\,\mu\text{m}^2$; five slices were acquired, each 900-μm thick, and one single field-of-view saturation slice suppressing signals from the head's ventral part was applied. The TR/TE for UF-IDE and IDE were 1500/35 and 750/35 ms, respectively. Thirty-two dummy scans were applied to reach a stable magnetization steady state. A b-value of 1000 s/mm^2 was achieved using an IDE waveform duration of 13.6 and 5.7 ms before and after the refocusing pulse, respectively, with a gradient peak amplitude of 610 mT/m. Another identical UF-IDE experiment with 400 repetitions was acquired to assess the potential benefits of a recently developed denoising scheme (43).

Analysis

Analysis in this study was performed using home-written code in MATLAB (The MathWorks, Natick, MA). All images were analyzed with the raw data, without any further postprocessing. The full diffusion tensor was obtained from nonlinear fitting of the DTI data, and MD was calculated from the average of the eigenvalues. The IDE and UF-IDE experiments provided the MD directly from $MD_{IDE} = -\frac{1}{b}\log(S(b)/S(b=0))$ and $MD_{UF-IDE} = -\frac{1}{b}\log\left(\frac{S_2}{S_1 - N_{12}}\right)$, respectively, where $N_{12} = S_1 - S_2(G=0)$ is obtained from the scout. One in vivo data set was denoised slice-by-slice using random matrix theory (43), implemented in MATLAB (window size $= [8\ 8]$ voxels).

INDI Sensitivity Simulations

This analysis aims to quantify the sensitivity of INDI with its equal temporal resolution dMRI counterpart. Non-diffusion-weighted INDI signals were computed through $S_{INDI} = \cos(\pi/4) * (1 - e^{TR/T_1})$ for a broad range of TRs between 0.5 and 5 s and biologically relevant T_1s between 0.5 and 2.5 s. The corresponding time-matched dMRI signals with half the TR to maintain the same temporal resolution, were computed as $S_{dMRI} = \left(1 - e^{\frac{TR}{2T_1}}\right)$. All simulations assume that magnetization has been prepared in a steady state by dummy scans.

RESULTS

The principles of INDI were first tested on a simple doped water phantom. Assuming $T_1 >> T_{EPI/2} + T_{spoil}$ (Fig. 1), S_1 and $S_2(G=0\ \text{mT/m})$ should ideally be identical for $\alpha = 45^\circ$ and $\beta = 90^\circ$; however, the two images are not exactly equal in practice (Figs. 2a and 2b). S_2 signal intensity was typically somewhat weaker and spatially less homogeneous than S_1, particularly in the phantom experiments, likely because of its very short T_1/long T_2 that can exacerbate effects of uncrushed coherence pathways, as well as potential B_1 inhomogeneities, particularly for the $\pi/4$ pulse. Figure 2c shows the subtraction of the two signals, more clearly evidencing these differences (however, note that for example, in the in vivo experiments, the difference in these scout signals was much less pronounced, at approximately 5%).

Validation of INDI in a phantom
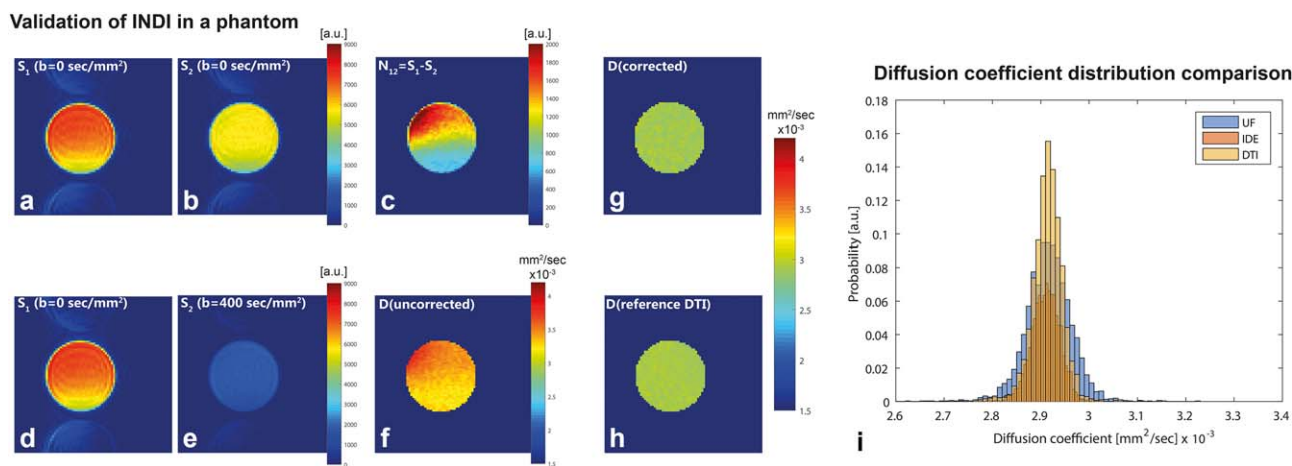
FIG. 2. Experimental validation of INDI in a phantom. **a, b**: Raw data for the scout INDI image, representing S_1 and S_2 in the absence of diffusion weighting (ideally, $S_1 = S_2$). **c**: The difference image, N_{12}, clearly shows that the echoes are not ideally matched. **d, e**: Raw data for INDI (specifically, UF-IDE). The signal in (**e**) is significantly attenuated by diffusion. **f**: Mean diffusivity derived directly from the images in (**d**) and (**e**). The map is inhomogeneous, and the diffusion coefficient is larger than expected. **g**: Mean diffusivity calculated using a correction from the scout image, showing a homogenous image of the tube, as expected. **h**: Ground-truth MD from DTI. Note that there is excellent agreement between the maps in (**g**) (single-shot experiment) and (**h**) (12 different experiments are separated by a single TR for every image acquired). **i**: The UF-IDE, IDE, and DTI histograms are clearly overlapping, suggesting excellent agreement among the methods and noisier data for UF-IDE, as expected, at the fully relaxed condition.

Figures 2d and 2e show the raw data for a particular instantiation of INDI (i.e., the UF-IDE experiment), showing the attenuation of S_2 by diffusion weighting. Figure 2f shows the MD calculated directly from these raw images, without any correction applied. The uncorrected MD map suffers from two outstanding issues: (i) an artifactual spatial variation, unexpected for a homogeneous solution; and (ii) higher than expected MD values at this temperature. However, a simple subtraction of the scout image, N_{12}, from S_1 (as described in the Methods) completely remedies these discrepancies: The scout-corrected MD coefficient map (Fig. 2g) is both homogeneous across the slice, and depicts the correct diffusion coefficient values as obtained from the gold standard DTI (Fig. 2h). Figure 2i and Supporting Table S1 further quantify the distribution of diffusion coefficients within the sample as obtained from the gold-standard DTI, a conventional IDE, and the new UF-IDE sequence. Clearly, all methods are in excellent agreement in this free diffusion scenario; however, as expected, a higher variance is observed for the UF-IDE as a result of its inherently lower SNR in the fully relaxed regime.

To test the applicability of INDI in a biological system, we performed similar experiments in ex vivo brains. Figure 3a shows MD maps derived from UF-IDE (corrected with the N_{12} scout image) and from standard IDE in a representative brain. The UF-IDE and conventional IDE experiments result in very similar MD maps, although the SNR is somewhat lower for UF-IDE in this fully relaxed condition. Histograms from the entire brain are plotted in Figure 3b, whereas the median MD values arising from the different methods in the brain are tabulated in Supporting Table S1. The histograms are very similar for UF-IDE and IDE, as are the median MD values. The true correspondence between UF-IDE and its reference IDE was investigated by plotting the MD values in each voxel from the IDE experiments and their UF-IDE counterparts (Fig. 3c).

The plots are well-correlated (Pearson's $\rho = 0.71$) with very high significance (uncorrected $P < 1E-7$).

To ensure that UF-IDE can deliver robust images in vivo with high temporal resolution, experiments were performed on a mouse with a temporal resolution of 1.5 s (Fig. 4). The raw data (Fig. 4a) exemplify that the quality of UF-IDE data are comparable with the corresponding temporally-matched IDE, with approximately 20% higher SNR for the former. When denoised with random matrix theory (43), the image quality becomes even better, with SNR gains up to a factor of approximately 2 (Fig. 4a). The corresponding MD maps extracted from these experiments are shown in Figure 4b for a single slice and in Supporting Figure S1 for the rest of the slices acquired. The images are of high quality, considering the very high repetition rate. Histograms comparing the methods (Fig. 4c) overlap significantly, and the correlation between UF-IDE and IDE (Fig. 4d) is highly significant (Pearson's $\rho = 0.43$, uncorrected $P < 1E-7$).

To more directly compare the SNR properties of INDI and its conventional dMRI counterpart, Figures 5a and 5b illustrate non-diffusion-weighted signals (proportional to SNR up to a constant factor) for each method, for a broad range of TRs and biologically relevant T_1s. Clearly, dMRI overperforms INDI for very long TRs; however, as TRs are decreased to approximately 1–2 s, the differences between the sequences' SNR becomes much less apparent. To analyze potential SNR enhancements by INDI, Figure 5c computes the ratio of S_{INDI}/S_{dMRI}. For short TRs invariably required in high temporal resolution applications, the dominance of hot colors shows a marked advantage of INDI over the equivalent dMRI experiment. Quantitatively, INDI will provide SNR gains as long as TR is less than approximately $1.76T_1$ (dashed line in Fig. 5c), although it should be noted that if INDI's scout images suffer signal loss, it will proportionally penalize SNR. Nevertheless, in our in vivo experiments, this was not an issue, and, in excellent

MD Maps in the ex-vivo brain

a

Mean diffusivity histograms

b

Voxel correlations between IDE and UF-IDE

c
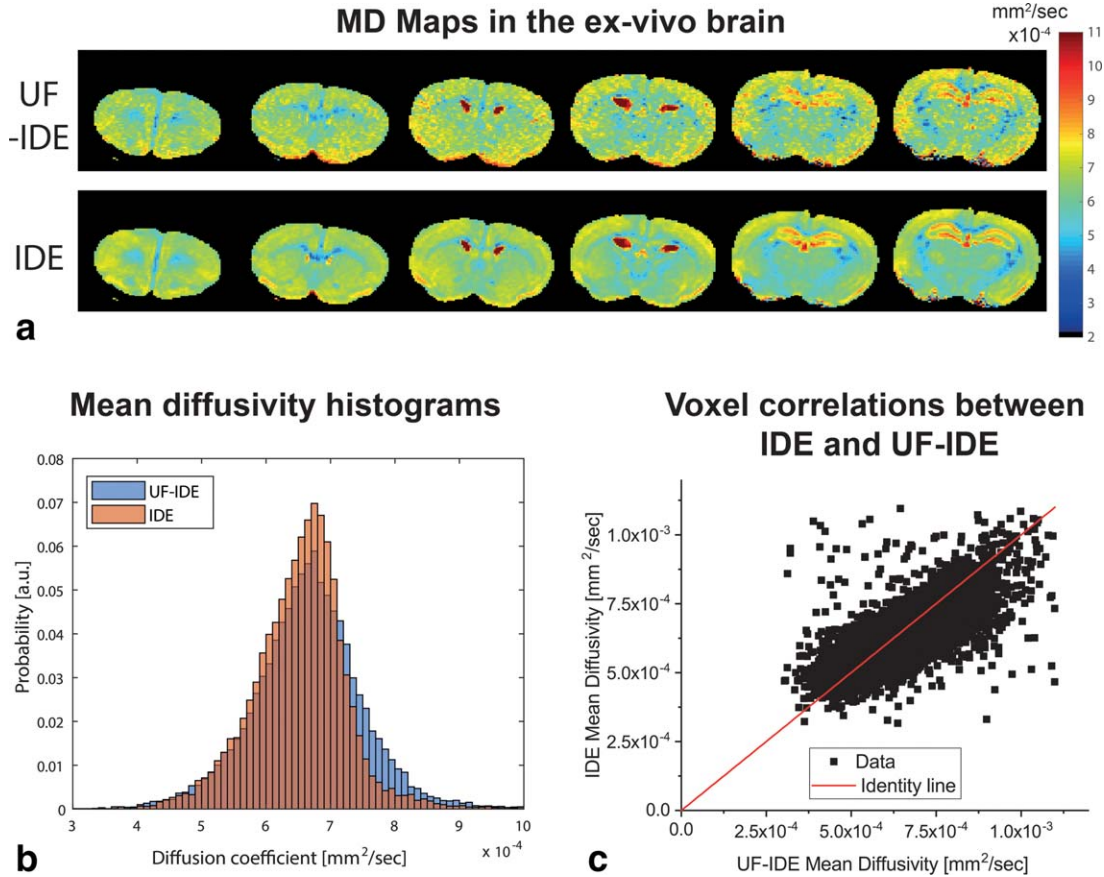
FIG. 3. Validation of INDI in ex vivo brain. **a**: Mean diffusivity maps from UF-IDE and IDE, showing comparable MD for UF-IDE and IDE. **b**: Histogram analysis shows very similar distribution of MD for UF-IDE and IDE. **c**: Correlation plot for UF-IDE and IDE shows very good correspondence between the voxels acquired with different methods. All brain (but not surrounding) voxels were pooled together for both panels.

In-vivo INDI

a

b

c

d
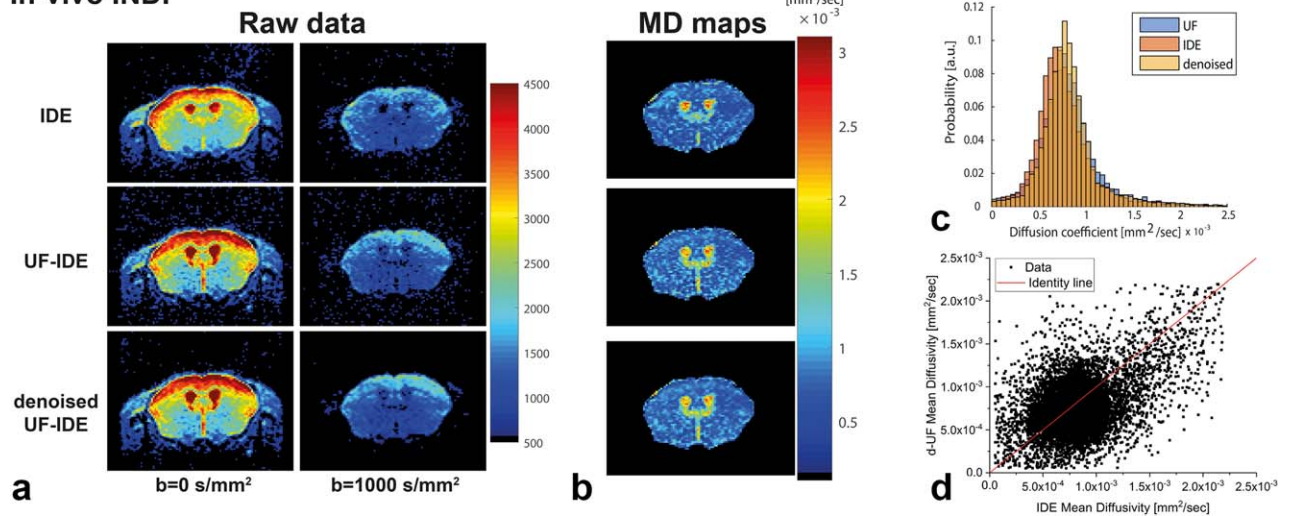
FIG. 4. INDI in vivo. **a**: Raw data from a representative slice of the mouse brain acquired at 9.4 T, for conventional IDE (acquired with TR = 750 ms), UF-IDE, and denoised IDE (d-IDE), acquired with TR = 1500 ms, but having the same temporal resolution as the conventional IDE. Excellent image quality was observed. **b**: Corresponding MD maps. The single-shot experiments are of good quality. **c**: Histogram distributions for the different methods for all brain (but not surrounding) voxels. The methods provide nearly identical distributions. **d**: Correlation analysis of IDE and d-UF IDE reveals a good correlation among the methods.
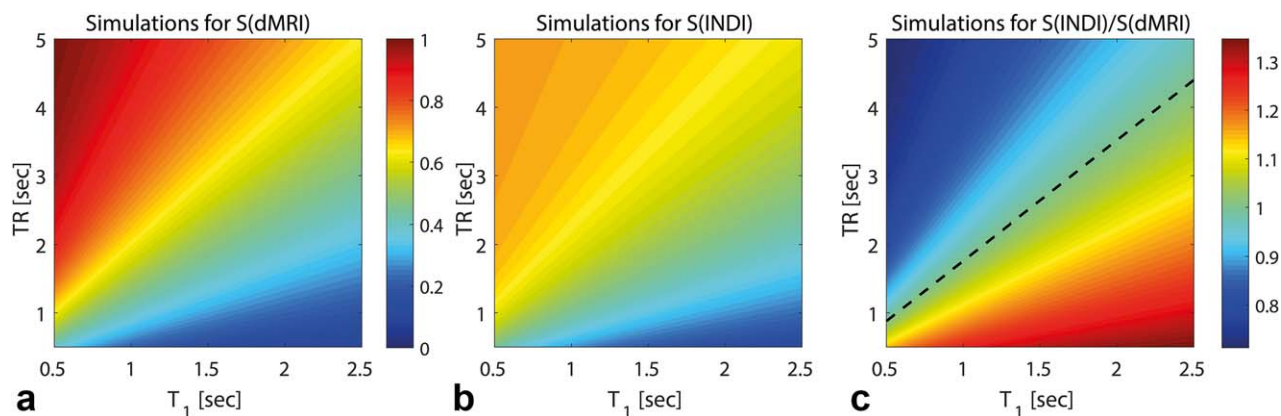
FIG. 5. Signal-to-noise ratio analysis for INDI and conventional dMRI. Simulated signals for conventional dMRI (**a**) and INDI (**b**) over a wide range of practical TR values and T_1 values are typical for biological tissues with field strengths between 1 and 16.4 T. Assuming constant noise with a standard deviation of one, the SNR profile of the two acquisitions is directly proportional to the signal maps. **c**: The INDI/dMRI signal ratios. The dashed line shows the point where dMRI and INDI have theoretically the same SNR, given that the two required images for each method are acquired with the same temporal resolution. The INDI method has a significant advantage when TR is less than approximately $1.76 \cdot T_1$.

agreement with the predictions of Figure 5c (TR of 1.5 s and T_1 of ~1.8 s), the nondenoised INDI acquisition indeed has an SNR gain of 1.20 to 1 when compared with the time-matched IDE. Thus, INDI can be used to acquire the baseline and diffusion-weighted images milliseconds apart, at least without suffering SNR loss, and potentially even with a modest SNR enhancement.

DISCUSSION

Dynamic changes in tissue ADC are at the core of diffusion fMRI methods, aiming to map functional signals more intimately related with neural activity compared with their BOLD counterparts (30,31,44). Disentangling changes in diffusion-driven metrics from changes in T_2 on the TR timescale could potentially improve the characterization of dynamic microstructural changes. Here, we have described INDI, a single-shot acquisition scheme with an inherent robustness against T_2 changes occurring on the TR timescale. By harnessing a partial initial nutation of the magnetization to encode the baseline image, it is possible to acquire the diffusion-weighted image only milliseconds later using the unperturbed magnetization reservoir. The TR is then fruitfully used to recover magnetization and reduce T_1 weighting. The INDI features were exemplified in a water phantom, in which a single, time-independent diffusion coefficient exists, and was accurately extracted from UF-IDE experiments. Both ex vivo and in vivo brain experiments evidenced very good correspondence between IDE and UF-IDE data.

It is instructive to consider INDI's SNR regimes. For initial conditions satisfying fully relaxed magnetization, the ideal INDI as prescribed here will incur a penalty of $\cos\left(\frac{\pi}{4}\right) = \frac{\sqrt{2}}{2}M_0$, whereas the corresponding dMRI will of course make use of the entire M_0. However, rapid acquisition schemes invariably entail non–fully relaxed conditions, in which INDI's magnetization (assumed to be set to an initial steady state by dummy scans) will have decayed by a factor of $\frac{\sqrt{2}}{2} * \left(1 - e^{-\frac{TR}{T_1}}\right)$, whereas the temporally equivalent dMRI would decay by $1 - e^{-\frac{TR}{2T_1}}$; the factor of 0.5 in the latter exponential accounts for

acquiring two dMRI images with identical temporal resolution as INDI. Theoretically, it can be shown that for $TR <\sim 1.76 T_1$, $S_{INDI} > S_{dMRI}$, and as shown in Figure 5c, for most biologically relevant conditions, INDI could even entail moderate sensitivity enhancements.

The INDI scout images also deserve some discussion for their temporal stability. The scout is used to normalize each pair of INDI images along a time series, thereby implicitly assuming that motion effects are negligible. However, in some applications, such as heart imaging, this assumption may be severely violated. In these cases, several scout images could be acquired in cine mode (i.e., with their cycle phase-locked to some external trigger and every INDI experiment measured along the cycle corrected with its phase-locked counterparts scout). Another alternative is to entirely forego the scout. Although the absolute value of MD may be biased, its time course may still be of significant value, as the bias should be constant, assuming that T_2 does not vary on the millisecond timescale. Finally, although we presented scout images with $\alpha = 45°$ and $\beta = 90°$, the difference between the baseline images can be made even smaller if the specific values for the first and second nutation pulses are tweaked (data not shown). For example, although we showed worst-case scenarios for the tube of water, the brain's scout images differed by approximately 5%, which could be mitigated even further with tweaking of the nutation angles (data not shown). If a good balance between the scout's S_1 and S_2 is achieved, then the scout images are not required, and the INDI experiment can proceed without the normalization step.

Here, we focused on a specific implementation of INDI (i.e., the UF-IDE sequence), and demonstrated its feasibility and utility for assessing MD. However, INDI can be used with any gradient waveform such as double-diffusion encoding ([14,15,45]) or nonuniform oscillating-gradient spin echo (46).

In conclusion, the INDI pulse sequence was presented and revealed its capability of mapping accurate diffusion coefficients with good sensitivity and excellent temporal resolution. The feasibility of INDI in preclinical settings

was demonstrated, and its immunity toward rapid changes in T_2 are promising for future dfMRI experiments and other applications calling for rapid mapping of microstructural dynamics.

ACKNOWLEDGMENTS

REFERENCES

1. Ogawa S, Kay AR, Tank DW. Brain magnetic resonance imaging with contrast dependent on blood oxygenation. Proc Natl Acad Sci 1990; 87:9868–9872.
2. Ogawa S, Lee T-M, Stepnoski R, Chen W, Zhu X-H, Ugurbil K. An approach to probe some neural systems interaction by functional MRI at neural time scale down to milliseconds. Proc Natl Acad Sci 2000; 97:11026–11031.
3. Yu X, Qian C, Chen DY, Dodd SJ, Koretsky AP. Deciphering laminar-specifc neural inputs with line-scanning fMRI. Nat Methods 2014;11:55–58.
4. Logothetis, NK, Pauls J, Augath M, Trinath T, Oeltermann A. Neurophysiological investigation of the basis of the fMRI signal. Nature 2001;412:150–157.
5. Logothetis NK. What we can do and what we cannot do with fMRI. Nature 2008;453:869–878.
6. Frydman L, Blazina D. Ultrafast two-dimensional nuclear magnetic resonance spectroscopy of hyperpolarized solutions. Nat Phys 2007;3:415–419.
7. Ma D, Gulani V, Seiberlich N, Liu K, Sunshine JL, Duerk JL, Grwiswold MA. Magnetic resonance fingerprinting. Nature 2013;495:187–192.
8. Frydman L, Scherf T, Lupulescu A. The acquisition of multidimensional NMR spectra within a single scan. Proc Natl Acad Sci 2002;99: 15858–15862.
9. Stejskal EO, Tanner JE. Spin diffusion measurements: spin echoes in the presence of a time-dependent field gradient. J Chem Phys 1965;42:288.
10. Shemesh N, Jespersen SN, Alexander DC, et al. Conventions and nomenclature for double diffusion encoding NMR and MRI. Magn Reson Med 2015;75:82–87.
11. Basser PJ, Mattiello J, LeBihan D. MR diffusion tensor spectroscopy and imaging. Biophys J 1994;66:259–267.
12. Tuch DS. Q-ball imaging. Magn Reson Med 2004;52:1358–1372.
13. Tournier JD, Calamante F, Gadian DG, Connelly A. Direct estimation of the fiber orientation density function from diffusion-weighted MRI data using spherical deconvolution. Neuroimage 2004;23:1176–1185.
14. Mitra PP. Multiple wave-vector extensions of the nmr pulsed-field-gradient spin-echo diffusion measurement. Phys Rev B Condens Matter 1995;51:15074–15078.
15. Shemesh N, Cohen Y. Microscopic and compartment shape anisotropies in gray and white matter revealed by angular bipolar double-PFG MR. Magn Reson Med 2011;65:1216–1227.
16. Lawrenz M, Finsterbusch J. Mapping measures of microscopic diffusion anisotropy in human brain white matter in vivo with double-wave-vector diffusionweighted imaging. Magn Reson Med 2015;73:773–783.
17. Ianus A, Drobnjak I, Alexander DC. Model-based estimation of microscopic anisotropy using diffusion MRI: a simulation study. NMR Biomed 2016;29:627–685.
18. Assaf Y, Blumenfeld-Katzir T, Yovel Y, Basser PJ. AxCaliber: a method for measuring axon diameter distribution from diffusion MRI. Magn Reson Med 2008;59:1347–1354.
19. Alexander DC, Hubbard PL, Hall MG, Moore EA, Ptito M, Parker GJ, Dyrby TB. Orientationally invariant indices of axon diameter and density from diffusion MRI. Neuroimage 2010;52:1374–1389.
20. Ozarslan E, Koay CG, Shepherd TM, Komlosh ME, Irfanoglu MO, Pierpaoli C, Basser PJ. Mean apparent propagator (MAP) MRI: a novel diffusion imaging method for mapping tissue microstructure. Neuroimage 2013;78:16–32.
21. Jones DK, editor. Diffusion MRI: theory, methods and applications. Oxford, United Kingdom: Oxford University Press; 2011.
22. Moseley ME, Cohen Y, Mintorovitch J, Chileuitt L, Shimizu H, Kucharczyk J, Wendland MF, Weinstein PR. Early detection of regional cerebral ischemia in cats: comparison of diffusion- and T2-weighted MRI and spectroscopy. Magn Reson Med 1990;14:330–346.
23. Warach S, Gaa J, Siewert B, Wielopolski P, Edelman RR. Acute human stroke studied by whole brain echo planar diffusion-weighted magnetic resonance imaging. Ann Neurol 1995;37:231–241.
24. Merino JG, Warach S. Imaging of acute stroke. Nat Rev Neurol 2010; 6:560–571.
25. Seunarine KK, Alexander DC. Multiple fibres: beyond the diffusion tensor. In: Behrens TE, editor. Diffusion MRI: from quantitative measurement to in vivo neuroanatomy. Cambridge, MA: Academic Press; 2009. pp 56–74.
26. Sagi Y, Tavor I, Hofstetter S, Tzur-Moryosef S, Blumenfeld-Katzir T, Assaf Y. Learning in the fast lane: new insights into neuroplasticity. Neuron 2012;73:1195–1203.
27. Horsfield MA, Jones DK. Applications of diffusion-weighted and diffusion tensor MRI to white matter diseases—a review. NMR Biomed 2002;15:570–577.
28. Padhani AR, Liu G, Mu-Koh D, et al. Diffusion-weighted magnetic resonance imaging as a cancer biomarker: consensus and recommendations. Neoplasia 2009;11:102–125.
29. Le Bihan D. Looking into the functional architecture of the brain with diffusion MRI. Nat Rev Neurosci 2003;4:469–480.
30. Tsurugizawa T, Ciobanu L, Le Bihan D. Water diffusion in brain cortex closely tracks underlying neuronal activity. Proc Natl Acad Sci 2013;110:11636–11641.
31. Tsurugizawa T, Abe Y, Le Bihan D. Water apparent diffusion coefficient correlates with gamma oscillation of local field potentials in the rat brain nucleus accumbens following alcohol injection. J Cereb Blood Flow Metab 2016. doi: 10.1177/0271678X16685104
32. Aso T, Urayama S, Poupon C, Sawamoto N, Kukuyama H, Le Bihan D. An intrinsic diffusion response function for analyzing diffusion functional MRI time series. Neuroimage 2009;47:1487–1495.
33. Miller KL, Bulte DP, Devlin H, Robson MD, Wise RG, Woolrich MW, Jezzard P, Behrens TE. Evidence for a vascular contribution to diffusion FMRI at high b value. Proc Natl Acad Sci U S A, 2007;104:20967–20972.
34. Mori S, Van Zijl PC. Diffusion weighting by the trace of the diffusion tensor within a single scan. Magn Reson Med 1995;33:41–52.
35. Topgaard D. Isotropic diffusion weighting using a triple-stimulated echo pulse sequence with bipolar gradient pulse pairs. Microporous Mesoporous Mater 2015;205:48–51.
36. de Graaf RA, Braun KPJ, Nicolay K. Single-shot diffusion trace 1H NMR spectroscopy. Magn Reson Med 2001;45:741–748.
37. Wong EC, Cox RW, Song AW. Optimized isotropic diffusion weighting. Magn Reson Med 1995;34:139–143.
38. Tang XP, Sigmund EE, Song YQ. Simultaneous measurement of diffusion along multiple directions. J Am Chem Soc 2004;126:16336–16337.
39. Eriksson S, Lasic S, Topgaard D. Isotropic diffusion weighting in PGSE NMR by magic-angle spinning of the q-vector. J Magn Reson 2013;226:13–18.
40. Topgaard D. Isotropic diffusion weighting in PGSE NMR: numerical optimization of the q-MAS PGSE sequence. Microporous Mesoporous Mater 2013;178:60–63.
41. Petiet A, Santin M, Bertrand A, et al. Gadolinium-staining reveals amyloid plaques in the brain of Alzheimer's transgenic mice. Neurobiol Aging 2012;33:1533–1544.
42. Topgaard D. Director orientations in lyotropic liquid crystals: diffusion MRI mapping of the Saupe order tensor. Phys Chem Chem Phys 2016;18:8545.
43. Veraart J, Fieremans E, Novikov DS. Diffusion MRI noise mapping using random matrix theory. Neuroimage 2016;76:1582–1593.
44. Abe Y, Tsurugizawa T, Le Bihan D. Water diffusion closely reveals neural activity status in rat brain loci affected by anesthesia. PLoS Biol 2017;15:e2001494.
45. Cheng Y, Cory D. Multiple scattering by NMR. J Am Chem Soc 1999; 121:7935–7396.
46. Shemesh N, Alvarez GA, Frydman L. Measuring small compartment dimensions by probing diffusion dynamics via non-uniform Oscillating-Gradient Spin-Echo (NOGSE) NMR. J Magn Reson 2013;237:49–62.

SUPPORTING INFORMATION

Additional Supporting Information may be found in the online version of this article.

Fig. S1. Initial nutation diffusion imaging maps in vivo for all slices. Top to bottom rows represent IDE, UF-IDE, and the denoised UF-IDE MD maps, respectively.